

Kinetic Monte Carlo simulations of ionic conductivity in oxygen ion conductors

Philipp Hein ^a, Benjamin O.H. Grope ^a, Julius Koettgen ^{a,c,*}, Steffen Grieshammer ^{a,b,**}, Manfred Martin ^{a,b,c,d,***}

^a Institute of Physical Chemistry, RWTH Aachen University, Landoltweg 2, 52056, Aachen, Germany

^b Helmholtz-Institut Münster (IEK-12), Forschungszentrum Jülich GmbH, Corrensstraße 46, 48149, Münster, Germany

^c JARA-HPC, RWTH Aachen University and Forschungszentrum Jülich GmbH, Landoltweg 2, 52056, Aachen, Germany

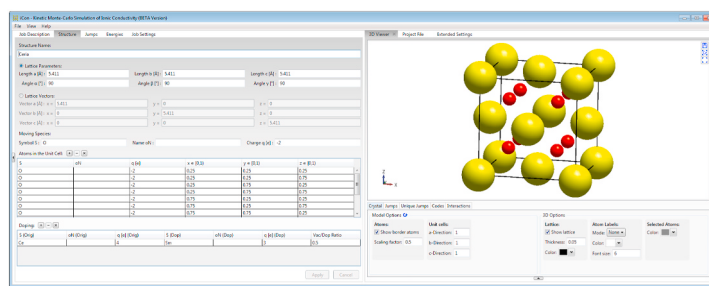
^d JARA-Energy, RWTH Aachen University and Forschungszentrum Jülich GmbH, Landoltweg 2, 52056, Aachen, Germany



HIGHLIGHTS

- Software for simulation of ionic conductivity.
- Kinetic Monte Carlo algorithm for arbitrary crystal structures.
- Simulation of ionic conductivity in solid-state conductors based on *ab initio* energies.
- Simulations of doped cerium oxides agree with experiments.

GRAPHICAL ABSTRACT



ARTICLE INFO

Keywords:

Kinetic Monte Carlo
Ionic conductivity
Solid electrolytes
Resistive switching

ABSTRACT

Ionic conductivities of solid-state materials are crucial for the performance of various applications ranging from batteries and fuel cells to resistive switching devices. The macroscopic ionic conductivity results directly from the microscopic energy landscape of ion diffusion. Lattice site energies and migration barriers depend on lattice defects such as vacancies and dopant ions in the local environment. The multiplicity of possible defect interactions with the migrating ion impedes the use of analytic models. While *ab initio* methods allow the calculation of the microscopic energy barriers for individual jumps, calculations of the macroscopic conductivity are computational very demanding, especially for more than 250 different materials and their possible ionic configurations as presented in this study. Kinetic Monte Carlo simulations allow the simulation of the ionic conductivity based on *ab initio* data and bridge the gap between microscopic jump events and the macroscopic conductivity. In this work, we discuss the Kinetic Monte Carlo method and its application to oxygen ion conductors for the example of doped ceria. We demonstrate how Kinetic Monte Carlo simulations can be accelerated to be 100 times faster with preserved high accuracy. Moreover, we report how the accuracy of Kinetic Monte Carlo simulations is improved with a large interaction radius and minimal computational expenses.

* Corresponding author. Institute of Physical Chemistry, RWTH Aachen University, Landoltweg 2, 52056, Aachen, Germany.

** Corresponding author. Helmholtz-Institut Münster (IEK-12), Forschungszentrum Jülich GmbH, Corrensstraße 46, 48149, Münster, Germany.

*** Corresponding author. JARA-Energy, RWTH Aachen University and Forschungszentrum Jülich GmbH, Landoltweg 2, 52056, Aachen, Germany.

E-mail addresses: julius.koettgen@rwth-aachen.de (J. Koettgen), grieshammer@pc.rwth-aachen.de (S. Grieshammer), martin@rwth-aachen.de (M. Martin).

1. Introduction

The ionic conductivity in solid-state materials is one of the key properties determining material performance for a broad range of applications. In oxygen ion conductors, a common way to improve the ionic conductivity is doping with oxides of lower valent metals, whereby oxygen vacancies are created due to charge balance. A well-known example is the rare earth doped zirconia (YSZ) [1]. In solid oxide fuel cells and related electrochemical devices, the ionic conductivity of the electrolyte is crucial for the efficiency of the cell [2–4]. For catalytic applications, the mobility of the ions can be important to achieve high turnover frequencies. In recent years, resistive switching has gained increasing interest, e.g. for application in resistive random-access memories. For the common switching mechanisms of valence change memories, the ion migration, and polarization due to the applied voltage is the basic phenomenon [5–8]. Therefore, the understanding and prediction of the ionic conductivity and mobility in various structures are of general interest [9].

A solid ionic conductor can be represented as a framework of ions with fixed positions in the crystal lattice wherein the charge carriers, vacancies, and interstitials, are mobile. While the immobile ions only vibrate around their equilibrium positions, the mobile ions perform thermally activated jumps between defined lattice sites. Within the harmonic transition state theory, the jump rate Γ for each mobile ion is determined by an attempt frequency ν_0 and the energy barrier E_{mig} that must be crossed during the jump:

$$\Gamma = \nu_0 \cdot \exp\left(-\frac{E_{\text{mig}}}{k_B T}\right) \quad (1)$$

In the case of isotropic diffusion with uniform jump rates, the total mean squared displacement of a mobile ion can be calculated from the jump length \overline{l}^2 of an individual jump as

$$\overline{R}^2 = N_p \cdot \Gamma \cdot t \cdot \overline{l}^2, \quad (2)$$

where N_p is the number of different jumps \overline{l}_i available for the mobile ion. In the ideal lattice, where defect concentrations are very low and no defect interactions occur, jump rates and lengths are identical for all mobile ions. The diffusion coefficient depends on the dimensionality d and the mean squared displacement \overline{R}^2 of the mobile ions in the time span t :

$$D = \frac{\overline{R}^2}{2 \cdot d \cdot t} \quad (3)$$

In ‘ideal’ materials with a dilute concentration of vacancies or interstitials and without defect interactions, the macroscopic ionic conductivity can be derived directly from the microscopic ion motion. Here, the mobility u is related to the diffusion coefficient D by the Nernst-Einstein relation

$$u = qD/k_B T, \quad (4)$$

where k_B and T are the Boltzmann constant and absolute temperature, respectively. The ionic conductivity σ is given by the concentration c , charge q , and the electrochemical mobility u of the mobile ions:

$$\sigma = c \cdot q \cdot u \quad (5)$$

In contrast, at a non-dilute concentration of vacancies or interstitials, the motion of ions is correlated and depends on the local environment, which could be influenced not only by the interaction of the vacancies or interstitials with each other but also by the presence of dopant ions and other lattice defects. Typical examples are doped oxygen ion conductors with defect fractions of up to 10 or 20% such as doped ceria or stabilized zirconia. In this case, the macroscopic transport properties are given by the ensemble of mobile ions with various jump rates and a simple

analytical expression for the ionic conductivity does not exist. Lattice Kinetic Monte Carlo (KMC) simulations connect the microscopic jump processes with the macroscopic transport properties by tracking the statistical movement of the mobile ions along different migration paths with different migration energies, which can be derived from *ab initio* calculations, e.g. density functional theory (DFT). The dynamics are simplified such that the vibrations of the ions around their lattice positions are discarded and only the jumps between fixed lattice sites are considered with a pre-defined attempt frequency [10]. This approach allows simulations for systems with several thousand to millions of ions over a time span in the range of microseconds for a variety of materials to investigate the influence of composition and temperature on the ionic transport. Simulations of these types have been performed for doped ceria and other fluorite structured oxides in recent years with different energy models applied [11–21].

In this paper, we first summarize the theory of Kinetic Monte Carlo and then demonstrate its application to oxygen ion conductors using our Monte Carlo code *iCon*. We introduce the implementation details of the software, discuss possibilities of energy modeling and exemplify by the simulation of the ionic conductivity in doped cerium oxide.

2. Principles of Kinetic Monte Carlo

The Kinetic Monte Carlo (KMC) method simulates the statistical process of ion migration in a defined lattice by weighting kinetic probabilities through the generation of random numbers. According to Eq. (1), mobile ions attempt to jump to vacant neighboring sites with an attempt frequency ν_0 and perform the jump with a probability p depending on the migration energy E_{mig} :

$$p = \exp\left(-\frac{E_{\text{mig}}}{k_B T}\right) \quad (6)$$

There are two important implementations of the KMC method [22, 23]. In the ‘rejection based’ or ‘null-event’ algorithm one of all possible jumps is selected with a uniform probability in each simulation step [22]. The migration energy is determined depending on the jump environment. Then, a uniform distribution random number $Z \in [0, 1]$ is drawn. If Z is smaller than the probability p the jump is accepted. Otherwise it is rejected, and the algorithm starts with a new jump attempt. The time is advanced by a time step

$$\Delta t = -\frac{1}{\Gamma_{\text{tot}}} \ln(Z'), \quad (7)$$

where the total rate Γ_{tot} is the sum of the rates (cf. (1)) for all possible jumps and Z' is another uniform distribution random number $\in [0, 1]$.

In the ‘rejection-free’ or ‘rate-catalog’ approach the rates of all possible jumps are calculated and stored in a rate-catalog [23]. From this list, one transition is randomly selected with a probability proportional to the individual rate. The time is advanced by a time step according to Eq. (7) and the rate catalog is updated. In both implementations, the simulation is stopped if a certain criterion is fulfilled, e.g. a predefined number of successful Monte Carlo steps (N_{MCS}) is reached.

Despite some discussions about the validity of the rejection-based algorithm, the equivalence of both algorithms was shown [24, 25]. The efficiency of the particular algorithm depends on the temperature as well as the underlying energy model. The computational bottleneck for the ‘rejection based’ algorithm is the fact that a large number of jumps is rejected while for the ‘rejection-free’ algorithm the updating of the rate-catalog is limiting.

3. Simulation of ionic conductivity

3.1. Algorithm

In this work, we apply the ‘rejection-based’ algorithm during our

kinetic Monte Carlo simulations to obtain the ionic conductivity in single crystals.

In literature, the ionic conductivity is most often derived after calculating the diffusion coefficient of the mobile ions according to Eq. (3) and using then the Nernst-Einstein relation, although the latter is only valid in the dilute case [26]. To avoid the limitations imposed by the Nernst-Einstein relation, the conductivity can be directly obtained from the simulation by applying a weak electric field \vec{E} (cf. Fig. S1), which is a valid approach as shown in the literature [26–30]. Following the definition of the electrochemical mobility u , which is equal to the mean drift velocity per electric field strength, the mobility is then given by

$$u = \frac{\vec{R} \cdot \vec{E}}{|\vec{E}|^2 \cdot t}, \quad (8)$$

where $\vec{R} \cdot \vec{E} / |\vec{E}|$ is the mean displacement of all mobile ions in the direction of the electric field and t is the simulated time span [26].

The simulated time span is the sum of all individual time steps Δt (see Eq. (7)) depending on the total rate Γ_{tot} at a given time. However, since we are interested in the steady-state conductivity, we can calculate the simulated time from an expected probability as discussed in [appendix A](#). Then the time is calculated from the total number of jump attempts N_{att} divided by the number of mobile ions N_c , the number of available jump directions N_p for each mobile ion and the attempt frequency ν_0 as discussed in a previous publication [29]:

$$t = N_{MCS} \cdot \left(\sum_{j=1}^{N_c} \sum_{i=1}^{N_p} \Gamma_{ij} \right)^{-1} = \frac{N_{att}}{N_c \cdot N_p \cdot \nu_0} \quad (9)$$

In the presence of an electric field, the migration energies are modified according to

$$E'_{mig} = E_{mig} \pm \frac{q \cdot \vec{E} \cdot \vec{l}}{2}, \quad (10)$$

antiparallel (+) or parallel (−) to the field where $\vec{l} / 2$ is the vector from the position of the migrating charge carrier in the initial state to its position in the transition state assuming that the transition state is in the middle between initial and final state, which is correct for relatively small fields. Without the electric field, the mean displacement \vec{R} of the mobile ions is given by

$$\vec{R} = \frac{N_{MCS}}{N_c} \vec{r} = \frac{N_{att}}{N_c} \vec{r}_{att} = \frac{N_{att}}{N_c \cdot N_p} \sum_{i=1}^{N_p} \vec{l}_i \exp\left(-\frac{E_{mig}}{k_B T}\right) = 0, \quad (11)$$

where \vec{r}_{att} is the mean displacement of a single jump attempt. For isotropic diffusion, this equates to zero, since every jump vector is counterbalanced by one in the opposite direction. With an electric field, there is a non-zero net displacement in the direction of the field and a combination of [eqs. \(10\)](#) and [\(11\)](#) leads to:

$$\frac{\vec{R} \cdot \vec{E}}{|\vec{E}|} = \frac{N_{att}}{N_c \cdot N_p} \sum_{i=1}^{N_p} \frac{\vec{E} \cdot \vec{l}_i}{|\vec{E}|} \exp\left(-\frac{E_{mig}}{k_B T} + \frac{q \cdot \vec{E} \cdot \vec{l}_i}{2k_B T}\right) \quad (12)$$

For weak electric fields, the exponential term can be linearized with respect to $q \cdot \vec{E} \cdot \vec{l}_i / 2k_B T$ and [equation \(12\)](#) simplifies to¹:

$$\frac{\vec{R} \cdot \vec{E}}{|\vec{E}|} = \frac{N_{att}}{N_c \cdot N_p} \exp\left(-\frac{E_{mig}}{k_B T}\right) \frac{q |\vec{E}|}{2k_B T} \sum_{i=1}^{N_p} \frac{(\vec{E} \cdot \vec{l}_i)^2}{|\vec{E}|^2} \quad (13)$$

Since $\sum (\vec{E} \cdot \vec{l}_i)^2 / |\vec{E}|^2 = \sum \vec{l}_i^2 / d$ for isotropic diffusion, a combination of [eq. \(13\)](#) with [eqs. \(8\)](#) and [\(9\)](#) yields the same expression for the mobility u as [eqs. \(1\)–\(5\)](#). However, for variable migration energies, this analytic expression is no longer valid and KMC simulations are necessary to yield the mean displacement of all mobile ions, which jump in different local environments. Together with the simulated time, it is then possible to calculate the ionic mobility and conductivity according to [eq. \(8\)](#).

3.2. Transition rates

For the simulations, it is required to know all jump rates according to [eq. \(1\)](#). Here, we apply the common simplification that the pre-exponential factor ν_0 is a constant although the value might change depending on the local environment [31]. With ν_0 constant, the only variable is the migration energy E_{mig} which is the difference between the energies of initial state and transition state. Both energies depend on the respective crystallographic site and the local ionic environment, i.e. the occupation of lattice sites by regular ions, dopant ions, and oxygen vacancies. As the number of possible configurations gets enormous with increasing interaction radius, an appropriate energy model has to be applied (see below).

3.3. Electric field

To obtain the ionic conductivity directly from the simulation, a weak electric field is applied, as explained in [section 3](#) (cf. [Eqs. \(8\)](#) and [\(10\)](#)). For this purpose, the strength and the direction of the electric field \vec{E} must be defined. For strong electric fields, the mean displacement of the ions in the field is large and the migration statistics improve. However, the field has to be weak enough such that its influence is small compared to the migration energies and the linear approach in [eq. \(8\)](#) is still valid.

In our simulations, we define the electric field by the corresponding energy contribution in units of $k_B T$ which makes the field contribution in [Eq. \(12\)](#) independent of temperature. The field strength is then adjusted to the largest jump vector, such that $\max(q \cdot \vec{E} \cdot \vec{l}_i / 2)$ for all possible jump vectors \vec{l}_i equals the defined value. A value of 0.1 has proven to be a good choice for most of the investigated systems (cf. [Fig. S2](#)). The resulting typical field strength in the simulations (10^5 – 10^6 V cm^{−1}) is much higher than in most experiments, e.g. 10^{−1} V cm^{−1} during conductivity measurements.

3.4. Normalization

As the migrating ion has to overcome the migration barrier, only a small fraction of jump attempts leads to a successful transition in the rejection-based algorithm. For example, with a migration energy of 0.5 eV and a temperature of 500 K, on average only one out of 10^5 attempts is accepted. To accelerate the simulations, the migration energies are normalized such that the jump with the lowest possible migration energy is always accepted. The transition probability is then given by p / p_{max} where p is the Boltzmann probability from [eq. \(6\)](#) and $p_{max} = \exp(-\min(E_{mig}) / (k_B T))$. This normalization does not change the relative probability of the individual jumps and is compensated in the calculation of the simulated time span by modifying [eq. \(9\)](#):

$$t = \sum_{k=1}^{N_{MCS}} \frac{N_{att,k}}{N_{t,k} \cdot \nu_0 \cdot p_{max}} \quad (14)$$

¹ Here we implicitly assume that the energy barrier is equal for each jump vector \vec{l}_i . An analytic solution without this limitation is still possible as long as the barriers do not depend on the lattice site and migration is still isotropic.

$$N_{t,k} = \sum_{j=1}^{N_c} N_{p,k,j} \quad (15)$$

where $N_{p,k,j}$ is the number of jump directions of ion j for the k th Monte Carlo. However, the lowest possible migration energy can be very small compared to $k_B T$. In this case, no normalization is performed although the corresponding configuration might be unlikely and the associated jump may never occur.

An alternative option is the ‘dynamic normalization’ to the lowest migration energy that occurs in the simulation. Before the dynamic normalization, the lattice is (partially) equilibrated using a certain number of Monte Carlo steps. This removes improbable jump environments, which occur in the initial lattice due to the random distribution of dopants and vacancies. Subsequently, the migration energies of a defined number of jumps attempts are recorded. The dynamic normalization can now be performed using the lowest occurring or one of the lowest occurring energies. The dynamic normalization allows a more sophisticated acceleration of KMC simulations, while a minor physical error is introduced as all jumps with migration energies below the normalization energy now have the same jump probability and are always accepted. Nevertheless, with a reasonable setting of the normalization threshold, this error can be kept small and the simulation runtime can be reduced by several orders of magnitudes (cf. section 4).

3.5. Implementation

The Kinetic Monte Carlo algorithm as described above was implemented in the in-house software *iCon*. [32] Periodic boundary conditions are applied in all spatial dimensions to mimic an infinitely large lattice. Random numbers are generated by the MT19937 pseudo-random number generator [33]. The Fisher-Yates algorithm [34] is used to distribute dopants and vacancies randomly in the simulation cell. In every simulation step, a vacancy and an associated jump direction are chosen simultaneously to ensure that every jump in the lattice is selected with equal probability. Individual positions of the sub-lattice of the mobile species can have a different number of possible jump directions N_p and the vacancies can exchange between these positions. Therefore, the total number of possible jumps to neighboring positions may change during the simulation. As a result, the number of vacancies having a certain N_p is tracked over the whole simulation. In this way, not only all possible jumps can be chosen with the same probability, but also the simulated time span can be adapted to the total number of possible jumps. The simulated time span is then given by eqs. (14) and (15) instead of eq. (9), as shown in [appendix A](#). For each jump attempt, the occupations of the lattice positions in the jump environment are extracted and the migration energy is calculated from the defined energy model. The contribution of the electric field is added according to eq. (10) and the jump probability is obtained from eq. (6) using E_{mig} .

During the simulation, jumps may be rejected due to occupied or unstable sites. Both cases require special attention to reproduce the correct physical behavior. Firstly, the destination position of the chosen jump of a vacancy could be already occupied by another vacancy. The transition in this ‘site blocking’ situation is automatically denied but counts as a jump attempt. The classification of site blocking jumps as regular jump attempts originates from the definition of the simulated time span, which is calculated as the reciprocal sum of all jump rates (cf. eq. (9)). Here, the mean jump rate must decrease when site blocking increases, for example, due to a higher vacancy concentration. The mathematical treatment presented in [Appendix B](#) shows that site blocking can be handled in a physically correct way either by counting it as a jump attempt or by reducing the number of jump directions $N_{p,i}$ for the respective Monte Carlo step i accordingly. Following the approach of the KMC rejection algorithm, the first option is implemented in *iCon*. The site blocking effect is also the reason why in *iCon* vacancies are

randomly selected for jump attempts instead of equivalent mobile ions. Since the number of vacancies is typically lower than the number of mobile ions, this reduces the number of blocked jumps and thus the simulation runtime.

Secondly, jumps without a migration barrier might occur without normalization, for example, due to strong defect interactions in asymmetrically doped jump environments [35]. If the chosen jump has no migration barrier, the position of the vacancy before the chosen jump is unstable. As a result, the previous jump of this vacancy should have instantly moved the vacancy to the new position. Therefore, jumps with no migration barriers are not only always accepted but also do not count as a jump attempt (or Monte Carlo step). Moreover, *iCon* prevents jumps if they are immediately reversed. If the initial position of the vacancy is stable, i.e. the migration energy of a chosen jump is positive, the opposite direction of the jump can have no migration barrier. This renders the destination position of the chosen jump unstable and, even if the vacancy would have enough thermal activation to reach this position, it would immediately return to the initial position. As the lattice would remain unchanged, the transition is not valid and the jump is always rejected. This case is analog to the site blocking effect and must be either counted as a jump attempt, as implemented in *iCon*, or handled by reduction of $N_{p,i}$.

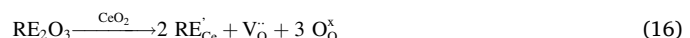
The simulation is divided into a preliminary and the main run, which are both terminated after a certain number of Monte Carlo steps per particle of the mobile species is reached. In the preliminary run, the initially random lattice is equilibrated. In the main run, the mean displacement \vec{R} of all mobile ions and the sum of the jump attempts $N_{\text{att},k}$ per number of available transitions $N_{t,k}$ are recorded to calculate the ionic conductivity with eqs. (8) and (14). For an example of the mean displacement as a function of time, see [Fig. S3](#).

4. Ionic conductivity of doped ceria

4.1. Simulation model

We examine doped ceria (CeO_2) as a suitable model system to study the influence of doping on the ionic conductivity. Ceria is known for its versatile applicability in solid oxide fuel cells, high-temperature batteries, and catalytic processes. Moreover, Gd-doped ceria has recently been investigated as resistive switching material in memristive devices [36]. Doped ceria has been subject to several Monte Carlo studies investigating defect distribution and ionic conductivity [4,17,29,30, 37–40].

Ceria crystallizes in the cubic fluorite structure with a lattice parameter of 5.41 Å and is comprised of a face-centered cubic sub-lattice of cerium ions with oxygen ions occupying the tetrahedral sites forming a primitive cubic sub-lattice. Doping with rare-earth oxides (RE_2O_3) leads to the formation of one vacancy in the oxygen sub-lattice per two dopant ions on cerium sites according to the following reaction (Kröger-Vink notation):



These oxygen vacancies enable the transport of oxygen ions by a vacancy hopping mechanism, where the vacancy changes its place with an oxygen ion in the nearest neighbor position along one of the lattice vectors ([Fig. 1](#) left). Jumps to farther positions are possible but can be neglected due to the large migration barriers [41].

In doped ceria, the migration energy for each jump is influenced by the interaction with neighboring dopant ions and oxygen vacancies. At the center of the jump between two tetrahedral sites, the oxygen ion crosses a migration edge formed by two cations. Calculations show that the doping of this edge with large dopant ions increases the migration barrier for both forward and backward jumps and, therefore, has a ‘blocking’ effect [4]. Additionally, oxygen vacancies experience an attractive interaction with the dopant ions leading to a ‘trapping’ effect,

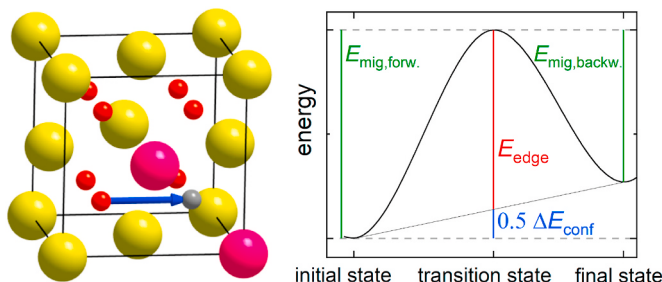


Fig. 1. Left: Section of cubic Sm-doped ceria showing an asymmetrically jump environment considered in the simulations. Cerium ions in light green, samarium ions in pink, oxygen ions in red and oxygen vacancy in gray. Right: Energy of the system as a function of the migration coordinate. The migration barriers are modeled using symmetric and asymmetric contributions. (For interpretation of the references to colour in this figure legend, the reader is referred to the Web version of this article.)

which increases the migration barrier for jumps away from the dopants and decreases the migration barrier for jumps towards the dopants. Furthermore, the repulsion between oxygen vacancies influences the migration barriers similarly but with opposite signs. A detailed discussion of these effects can be found in Ref. [4]. For the accurate simulation of the ionic conductivities, these effects are crucial and the cut-off radius for the interactions has to be chosen carefully, such that all important interactions are captured.

In the KMC simulations, the migration energy for each possible jump configuration has to be known. However, the number of possible configurations is vast. For ceria with a single dopant type (e.g. Sm), each cation position can be occupied by a cerium or dopant ion and each anion position can be occupied by an oxygen ion or vacancy. Considering only the six nearest cation positions and ten nearest anion positions around the jumping oxygen ion, a total of $2^{16} = 65,536$ configurations is possible leading to 16,675 unique configurations due to symmetry. Clearly, the calculation of all the migration barriers by DFT is not feasible and the energies have to be modeled by a limited set of parameters. In this work, we separate the interactions into a symmetric contribution (E_{sym}), which changes the migration barrier for a forward and backward jump by the same value and an asymmetric contribution (ΔE_{conf}), which changes both barriers by the same value but with opposite sign. The total barrier is then calculated as

$$E_{\text{mig}} = E_{\text{sym}} + 0.5 \Delta E_{\text{conf}} \quad (17)$$

where ΔE_{conf} is the energy difference between the initial and final state. An example of an energy profile is shown on the right side of Fig. 1. The contribution ΔE_{conf} is approximated from pair interactions between the migrating oxygen vacancy and the surrounding defects and is, therefore, an ‘additive’ contribution in the program. In contrast, E_{sym} is a

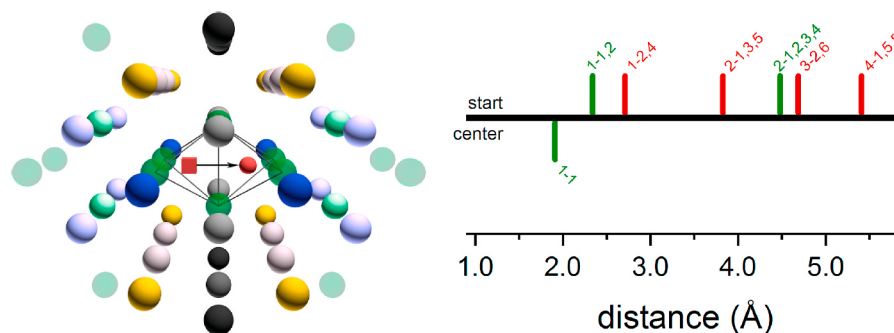


Fig. 2. Left: Cation shells around the migrating oxygen ion. Right: Distance of RE-V (green) and V-V (red) interactions from the initial position of the oxygen vacancy and the center of the jump. Numbers indicate the neighboring shell (1st, 2nd, etc.) in the respective sub-lattice before and after the jump. (For interpretation of the references to colour in this figure legend, the reader is referred to the Web version of this article.)

Table 1

Pair interaction energies and edge energies applied in the simulations according to Koettgen et al. [4]. For interaction 3NN II a cerium cation is located between the vacancies, while for 3NN I there is no cation. An attempt frequency of $1.47 \cdot 10^{12}$ Hz was chosen according to Koettgen et al. [31].

Pair interactions		
Defect pair	Distance (Å)	Energy (ev)
VV 1NN	2.7055	0.848
VV 2NN	3.8262	0.291
VV 3NN I	4.6861	0.306
VV 3NN II	4.6861	0.358
VV 4NN	5.4110	0.268
SmV 1NN	2.3430	-0.154
SmV 2NN	4.4866	-0.080
Edge energies		
Edge cations	energy (eV)	
Ce-Ce	0.466	
Ce-Sm	0.631	
Sm-Sm	1.031	

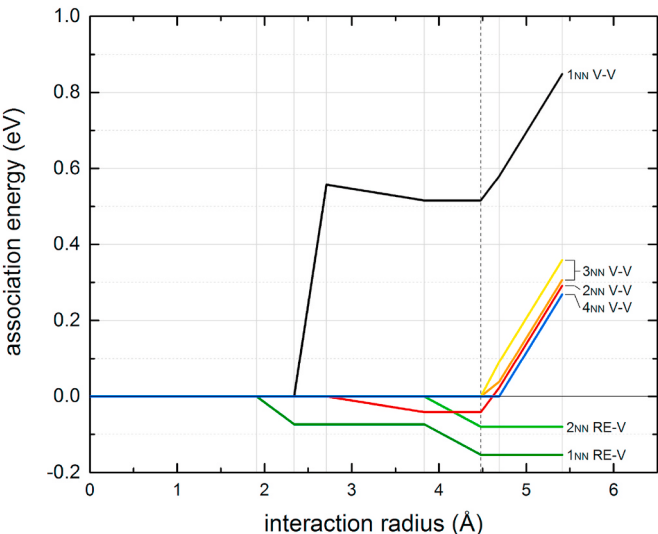


Fig. 3. Association energies as a function of the interaction radius. Note that the V-V repulsion does not monotonously decrease with the distance between the two oxygen vacancies. As a result, a V-V association can be observed depending on the interaction radius.

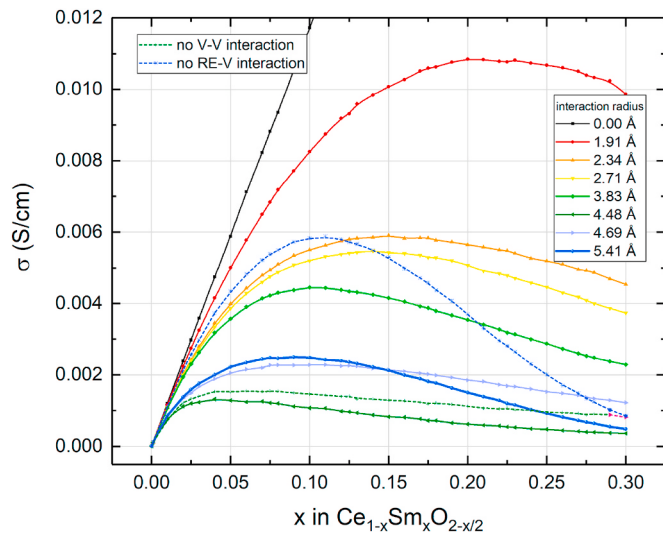


Fig. 4. Simulated conductivities as a function of the dopant fraction in Sm-doped ceria at 773 K for different interaction radii.

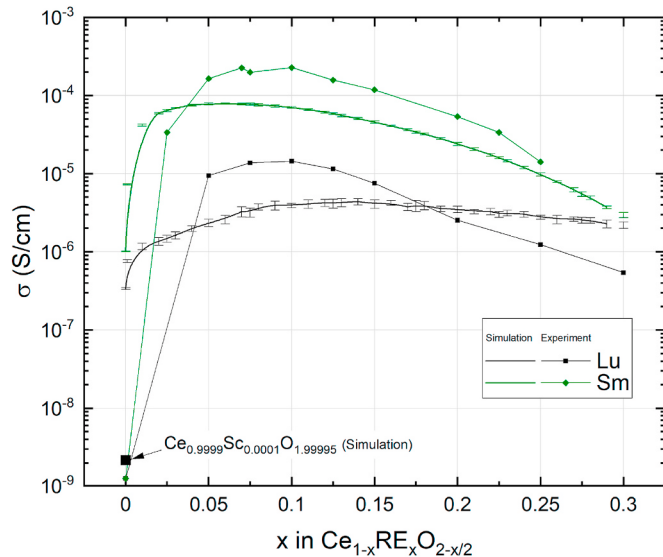


Fig. 5. Simulated and experimental bulk ionic conductivities at 267 °C of Lu and Sm doped ceria as a function of doping fraction. Additionally, the simulated ionic conductivity of $\text{Ce}_{0.9999}\text{Sc}_{0.0001}\text{O}_{1.99995}$ (Simulation) is shown. Lines are a guide to the eye only.

'permuted' contribution. This approach significantly reduces the number of DFT calculations as the large number of possible permutations is reduced to a limited set of pair interaction parameters ϵ_{ij} , which describe the interactions of the oxygen vacancy with the defect species j in a shell i around the initial or final position of the oxygen vacancy. During the simulation, only the numbers of these interactions in the initial (N_{ij}^{initial}) and the final state (N_{ij}^{final}) have to be determined, resulting in the contribution:

$$\Delta E_{\text{conf}} = \sum_{\substack{\text{shell } i \\ \text{species } j}} N_{ij}^{\text{final}} \epsilon_{ij} - \sum_{\substack{\text{shell } i \\ \text{species } j}} N_{ij}^{\text{initial}} \epsilon_{ij} \quad (18)$$

The simplest model that includes the effect of vacancy-dopant interactions has to include dopant ions at the migration edge. This contribution is symmetric as it shifts the barriers for a forward and backward jump in the same direction. For Sm-doped ceria, the

corresponding energies for the Ce-Ce, Ce-Sm, and Sm-Sm edges are 0.52 eV, 0.69 eV, and 1.09 eV, respectively [31]. Since the energy does not change linearly with the number of dopants, this contribution is permuted explicitly. Further cation sites around the jump are depicted on the left-hand side of Fig. 2. On the right-hand side of Fig. 2, the distance of the different cation and anion shells to the oxygen vacancy at the start or center position are shown, which are considered in this work. Identifiers in the form $A-B, C$ refer to the defect distance before the jump (A) and possible defect distances after the jump (B, C). For the simulations interaction energies calculated by means of DFT are taken from Ref. [4] and are given in Table 1 and Fig. 3.

4.2. Simulation results

Ionic conductivities of Sm-doped ceria ($\text{Ce}_{1-x}\text{Sm}_x\text{O}_{2-x/2}$) were simulated for dopant fractions x between 10^{-4} and 0.3 at a temperature of 773 K. Simulations were performed in a cell of $16 \times 16 \times 16$ unit cells with randomly distributed dopant ions, and an electrical field was applied corresponding to an energy contribution of $0.1 k_B T$. For each simulation, 100 MCS per oxygen ion were performed and 10 independent simulations were averaged for each data point. The attempt frequency was set to $v_0 = 1.47 \cdot 10^{12}$ Hz according to previous DFT calculations [31]. Different models with interaction radii between 0.0 Å and 5.41 Å were considered to investigate the influence of the interactions on the ionic conductivity.

The results are shown in Fig. 4. For an interaction radius of 0.0 Å, no interactions are considered at all and the migration energy is set to the value of the Ce-Ce edge. The conductivity increases with increasing dopant levels due to a higher vacancy concentration. The slight deviation from a linear increase of conductivity is due to the site-blocking effect since an oxygen vacancy cannot jump onto an already vacant site.

For an increasing interaction radius around the start, transition state and final positions of the migrating oxygen vacancy (see Fig. 1), interactions of the migrating oxygen vacancy with dopants (RE-V) and vacancies (V-V) are subsequently considered. At an interaction radius of 1.91 Å, the energies for the three different configurations of the cation edge are included. Due to the blocking effect of the doped edges, the conductivity is decreased and the conductivity curve as a function of the dopant fraction shows a distinct maximum in the simulated concentration range.

Increasing the interaction radius to 2.34 Å introduces the interactions with dopant ions around the initial and final position of the migrating oxygen vacancy. The energy for the jump of the oxygen vacancy is lowered for jumps towards the dopant (association) and increased for the jump away from it (dissociation). This trapping effect leads to a further decrease of the conductivity and a shift of the maximum to smaller values of x . The introduction of the vacancy-vacancy repulsion at 2.71 Å, further decreases the conductivity and shifts the maximum.

Increasing the interaction radius to 3.83 Å introduces a V-V repulsion, which is actually a V-V association, between next nearest neighborhood positions. As the V-V repulsion energy does not monotonously decrease with increasing V-V distance, an association of vacancies takes place. The conductivity decreases significantly. Increasing the interaction radius to 4.48 Å introduces a RE-V interaction between the next nearest neighborhood positions and increases the trapping effect. Similar to other association effects, the conductivity decreases significantly.

In summary, all interactions can decrease the conductivity: Increased symmetric migration barriers (blocking), RE-V association (trapping), V-V association, and even V-V repulsion. The influence on the conductivity increases with increasing dopant fraction.

However, this is not always the case: Increasing the interaction radius to 4.69 Å increases the conductivity. Here, any V-V interaction becomes repulsive and increases in energy. Obviously, V-V repulsion can also increase the conductivity. Increasing the interaction radius to

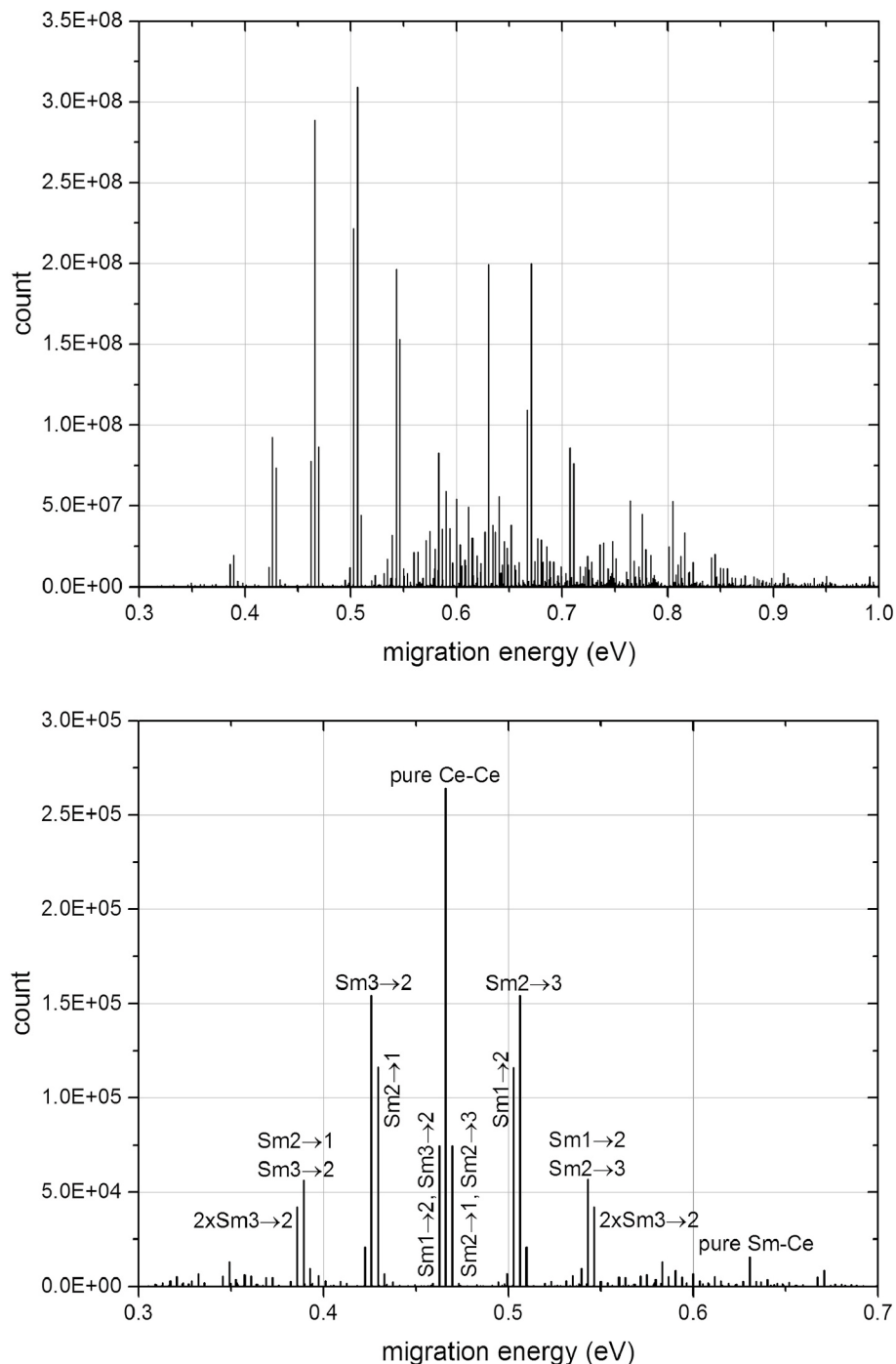


Fig. 6. Number of jump attempts N_{att} (top) and successful jumps (bottom) with a certain migration energy at 773 K in $\text{Ce}_{0.9}\text{Sm}_{0.1}\text{O}_{1.95}$. Annotations identify changes in the cation environment during each jump. For example, $\text{Sm}1\rightarrow 2$ identifies a jump where the oxygen vacancies are in the nearest neighbourhood to a Sm dopant before the jump and in the next nearest neighbourhood to a Sm dopant after the jump.

5.41 Å increases the V-V repulsion again significantly. However, the influence on the conductivity up to $x = 0.15$ is marginal. Here, the conductivity slightly increases. For larger dopant fractions the conductivity strongly decreases. While for small vacancy concentrations the V-V repulsion leads to an ordering of the vacancies that increases the conductivity, starting at intermediate vacancy concentrations the number of vacancies is too large leading to a decrease in conductivity.

Additionally, Fig. 4 shows the models without vacancy-vacancy interaction or dopant-vacancy interaction. Without the dopant-vacancy interaction, the conductivity increases due to the missing trapping effect. In contrast, without any vacancy-vacancy repulsion, the

conductivity slightly decreases. In this case, a strong trapping of several oxygen vacancies by a single dopant ion takes place since no repulsion between vacancies is included.

From the simulations, it is apparent that all considered interactions have a significant influence on both the magnitude of the conductivity and the position of the maximum, and, thus, the interaction radius has to be chosen carefully to capture all important effects. Moreover, we show how the accuracy of Kinetic Monte Carlo simulations is improved with a large interaction radius at minimal computational expenses in comparison to previous models of doped ceria [4]. A detailed comparison to experimental data is discussed in detail in our previous publications [4],

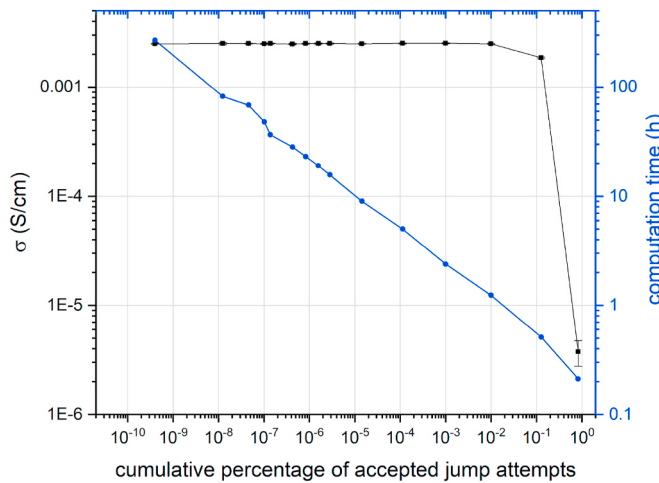


Fig. 7. Ionic conductivity and computation time for different settings of the dynamic normalization performed for $\text{Ce}_{0.91}\text{Sm}_{0.09}\text{O}_{1.955}$ at 773 K with the full model as stated in the text.

[42,43]. Fig. 5 shows the simulated and experimental bulk ionic conductivities at 267 °C of Sm, and for the first time, Lu doped ceria as a function of the doping fraction from our work. The simulated ionic conductivity of $\text{Ce}_{0.9999}\text{Sc}_{0.0001}\text{O}_{1.99995}$ is shown for comparison since experimental samples always contain a small concentration of impurities. KMC simulation and experiments are in agreement.

From the simulations, the jump statistics can be extracted. Fig. 6 shows the number of jump attempts (top) and successful jumps (bottom) in $\text{Ce}_{0.9}\text{Sm}_{0.1}\text{O}_{1.95}$ depending on the migration energy. While a large variety of jump attempts is visible, the successful jumps are dominated by jumps through the Ce–Ce edge without a change in the defect environment and, in addition, jumps with a change only in the cation environment. The main peaks in the diagram for the successful jumps are symmetric due to the detailed balance that is fulfilled in the simulations. In the thermodynamic equilibrium, the number of successful jumps into a configuration have to be identical to the number of successful jumps out of a configuration in order to keep the number of

oxygen vacancies in every configuration constant.

Depending on the model and dopant fraction, the runtime of the simulations in Fig. 4 ranged from minutes to a day per 100 MCS per oxygen ion or up to 30 ms per Monte Carlo step.

The run time can be drastically reduced by applying the dynamic normalization scheme as described above. Fig. 7 shows the influence of the dynamic normalization on the simulated ionic conductivity and the computation time in the case of $\text{Ce}_{0.91}\text{Sm}_{0.09}\text{O}_{1.955}$ at 773 K. In a first step, the probability and energy of all occurring jump configurations are recorded over $5 \cdot 10^9$ jump attempts. The configurations are ordered in ascending order of migration energies and the probabilities are cumulated. The normalization energy is chosen such that a given percentage of the jumps is always accepted. As shown in Fig. 7, the computation time can be decreased by a factor of about 100 without changing the obtained value of the conductivity. The ionic conductivity is not influenced within its error if a cumulative percentage of jump attempts up to 0.01% is accepted.

4.3. Further dopants

Ionic conductivities for further dopants were simulated and discussed in an earlier work for more than 250 materials [4]. The results for 773 K, shown in the contour plot in Fig. 8, clearly demonstrate that the maximum of the ionic conductivity depends on the ionic radius of the dopant and the dopant fraction. The highest conductivity is obtained for Sm-doped ceria with a dopant fraction of about 0.1. The absolute value of the RE-V association energy difference between nearest neighbor and next-nearest neighbor position is negligible for Nd doped ceria and increases for larger and smaller dopants. The absolute value of the RE-V association energy difference between the next nearest neighbor and third nearest neighbor position increases for larger dopants. As a result, Sm dopants have a low tendency to both catch and hold oxygen vacancies (catch-and-hold principle) [4]. The weak two-step trapping process leads to the high conductivity of Sm-doped ceria. For increasing dopant radius, the dopant fraction with the maximum conductivity decreases. The reason for the shift in the dopant fraction leading to the maximum in conductivity is the increasing blocking effect for larger dopants caused by an increase in the Ce-RE migration edge energy.

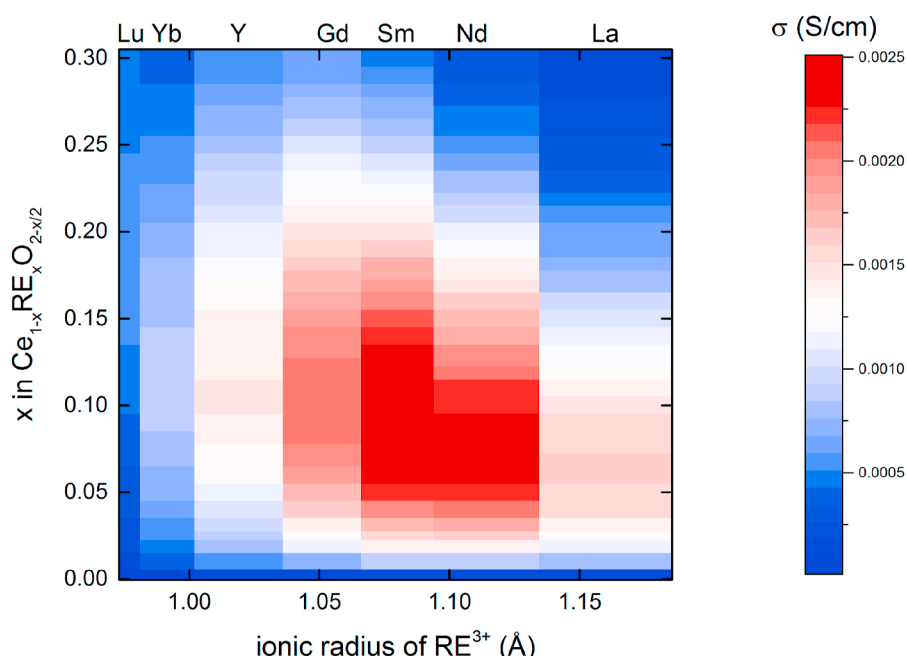


Fig. 8. Interpolated simulated ionic conductivity of ceria with different dopants at 773 K depending on the ionic radius of the dopant and the dopant fraction.

5. Conclusions

We present simulations of the oxygen ion conductivity in solid oxides based on the lattice Kinetic Monte Carlo (KMC) method using the software iCon. We discuss the algorithm and applicability for simulation of ionic conductivity with doped cerium oxide serving as a model system where the ionic conductivity depends on the dopant type and level of doping. The simulation results clearly show the influence of the blocking effect of dopant ions on the migration edge as well as the trapping due to the interaction of the moving oxygen vacancies with dopant ions or other oxygen vacancies. The interplay between these effects and the changing number of oxygen vacancies explains the conductivity maximum that is found in doped ceria. The simulated results are in agreement with experiments. We demonstrate how Kinetic Monte Carlo simulations can be accelerated to be 100 times faster with preserved high accuracy by applying the dynamic normalization. Moreover, we report how the accuracy of Kinetic Monte Carlo simulations is improved with a large interaction radius and minimal computational expenses. The potential to simulate systems with several thousand to millions of ions over a time span in the range of microseconds for a variety of materials to investigate the influence of composition and temperature on the ionic transport allows to select the most promising experiments and can accelerate the discovery of new and improved materials.

Author contributions

M.M. supervised the research project. P.H. and B.O.H.G. implemented the software package iCon. J.K. and S.G. conducted simulations for doped ceria. P.H., J.K., and S.G. prepared the manuscript.

Code availability

The simulations package iCon is available upon request. For more information, please visit www.iCon.pc.rwth-aachen.de.

CRediT authorship contribution statement

Philipp Hein: Methodology, Writing - review & editing. **Benjamin O.H. Grope:** Methodology. **Julius Koettgen:** Methodology, Investigation, Writing - original draft, Writing - review & editing. **Steffen Grieshamer:** Methodology, Investigation, Writing - original draft, Writing - review & editing. **Manfred Martin:** Conceptualization, Writing - review & editing.

Declaration of competing interest

The authors declare that they have no known competing financial interests or personal relationships that could have appeared to influence the work reported in this paper.

Acknowledgments

The authors gratefully acknowledge the computing time granted by the JARA-HPC Vergabegremium and provided on the JARA-HPC Partition part of the supercomputer JURECA at Forschungszentrum Jülich [44]. The authors gratefully acknowledge the computing time granted by the JARA-HPC Vergabegremium and provided on the JARA-HPC Partition part of the supercomputer CLAIX at RWTH Aachen University. Funding from the German Research Foundation (DFG) within the collaborative research center, SFB 917 “Nanoswitches”, is gratefully acknowledged.

Appendix C. Supplementary data

Supplementary data to this article can be found online at <https://doi.org/10.1016/j.matchemphys.2020.123767>.

Appendix A

A Kinetic Monte Carlo simulation is a stochastic process, where the states advance by discrete transitions. In the rejection-based algorithm, a possible transition is randomly chosen and then either accepted or rejected with its transition probability. These transitions are regarded as rare events in a Poisson process and thus the time Δt_k for the next Monte Carlo step k to occur is exponentially distributed. The expected value Δt_k is then given by the reciprocal total rate [23]:

$$\Delta t_i = \left(\sum_{j=1}^{N_{t,k}} \nu_0 \exp\left(-\frac{E_{mig,kj}}{k_B T}\right) \right)^{-1}, \quad (19)$$

where $N_{t,k}$ is the total number of possible transitions and $E_{mig,kj}$ is the migration energy of transition j for the Monte Carlo step k . The probability p_k for an accepted transition in the rejection-based algorithm is [22]:

$$p_i = \frac{1}{N_{t,k}} \sum_{j=1}^{N_{t,k}} \exp\left(-\frac{E_{mig,kj}}{k_B T}\right) \quad (20)$$

For each Monte Carlo step, the rejection-based algorithm is a Bernoulli process with success probability p_k , since the migration energies do not change until the next Monte Carlo step occurs. The number of required attempts $N_{att,k}$ is then geometrically distributed with the expected value $N_{att,k} = p_k^{-1}$. From eqs. (19) and (20) then follows for the simulated time span:

$$t = \sum_{i=k}^{N_{MCS}} \Delta t_k = \sum_{k=1}^{N_{MCS}} (\nu_0 \cdot N_{t,k} \cdot p_k)^{-1} = \sum_{k=1}^{N_{MCS}} \frac{N_{att,k}}{\nu_0 \cdot N_{t,k}} \quad (21)$$

For constant $N_{t,k}$ over the whole simulation, this simplifies to eq. (9). When $N_{t,k}$ changes, then eq. (21) must be used, where the ratio between transition attempts and available transitions must be recorded separately for each Monte Carlo step.

Appendix B

When some of the considered transitions in the rejection algorithm are temporarily or permanently impossible, then the number of available transitions $N_{t,k}$ is reduced for the respective Monte Carlo step k . Consequently, in this case, the impossible transitions should not be chosen in the algorithm, which means that the number of transition attempts is reduced as well. However, intuition also tells us that the simulation should be unaffected if additional highly improbable or impossible transitions are added to the algorithm. In the following, it is shown that this is indeed the case. Instead of reducing $N_{t,k}$, as explained above, it is equivalent to count the impossible transitions as attempts without reducing $N_{t,k}$. Since the impossible transitions do not influence how the state advances during the simulation, only the simulated time span is affected.

In the case where we exclude the impossible transitions from the algorithm, the original number of available transitions $N_{t,k}$ is reduced by the number of impossible transitions $N_{t,k}^X$ in each Monte Carlo step i . The transition probability p_k for this Monte Carlo step, which is equal to the reciprocal of the expected number of transition attempts $N_{att,k}$ required for the Monte Carlo step, is then given by:

$$p_k = N_{att,k}^{-1} = \frac{1}{N_{t,k} - N_{t,k}^X} \sum_{j=1}^{N_{t,k}} \exp\left(-\frac{E_{mig,kj}}{k_B T}\right) \quad (22)$$

Since the time span Δt_k for the Monte Carlo step is calculated as the reciprocal total rate, it is given by:

$$\Delta t_k = \left(\nu_0 \sum_{j=1}^{N_{t,k}} \exp\left(-\frac{E_{mig,kj}}{k_B T}\right) \right)^{-1} = \frac{N_{att,k}}{\nu_0 (N_{t,k} - N_{t,k}^X)}, \quad (23)$$

which is equivalent to eq. (9) but with a reduced number of transitions. When the impossible transitions are counted as attempts, then the transition probability is equal to the reciprocal sum of rejected transition attempts and impossible transition attempts, the latter being calculated from the rejected attempts and the ratio between impossible and possible transitions:

$$p_k = \frac{1}{N_{t,k}} \sum_{j=1}^{N_{t,k}} \exp\left(-\frac{E_{mig,kj}}{k_B T}\right) = \left(N_{att,k} + N_{att,k} \frac{N_{t,k}^X}{N_{t,k} - N_{t,k}^X} \right)^{-1} \quad (24)$$

Calculating the time span from the total rate then yields:

$$\Delta t_k = \left(\nu_0 \sum_{j=1}^{N_{t,k}} \exp\left(-\frac{E_{mig,kj}}{k_B T}\right) \right)^{-1} = \frac{N_{att,k} \left(1 + \frac{N_{t,k}^X}{N_{t,k} - N_{t,k}^X} \right)}{\nu_0 \cdot N_{t,k}}, \quad (25)$$

which again is equivalent to eq. (9), but this time with an increased number of attempts. eqs. (23) and (25) are equal, which is proof that both presented approaches for the handling of impossible transitions are similar.

References

- [1] B.C.H. Steele, A. Heinzel, Materials for fuel-cell technologies, *Nature* 414 (6861) (2001) 345–352.
- [2] J.B. Goodenough, Oxide-ion electrolytes, *Annu. Rev. Mater. Res.* 33 (1) (2003) 91–128.
- [3] J.B. Goodenough, Rechargeable batteries: challenges old and new, *J. Solid State Electrochem.* 16 (6) (2012) 2019–2029.
- [4] J. Koettgen, S. Grieshammer, P. Hein, B.O.H. Grope, M. Nakayama, M. Martin, Understanding the ionic conductivity maximum in doped ceria: trapping and blocking, *Phys. Chem. Chem. Phys.* 20 (2018) 14291–14321.
- [5] R. Waser, R. Dittmann, G. Staikov, K. Sotz, Redox-based resistive switching memories - nanoionic mechanisms, prospects, and challenges, *Adv. Mater.* 21 (25–26) (2009) 2632–2663.
- [6] D.S. Jeong, R. Thomas, R.S. Katiyar, J.F. Scott, H. Kohlstedt, A. Petraru, C. S. Hwang, Emerging memories: resistive switching mechanisms and current status, *Rep. Prog. Phys.* 75 (7) (2012), 076502.
- [7] Y. Aoki, C. Wiemann, V. Feyer, H.S. Kim, C.M. Schneider, H. Ill-Yoo, M. Martin, Bulk mixed ion electron conduction in amorphous gallium oxide causes memristive behaviour, *Nat. Commun.* 5 (2014) 3473.
- [8] D.-H. Kwon, S. Lee, C.S. Kang, Y.S. Choi, S.J. Kang, H.L. Cho, W. Sohn, J. Jo, S.-Y. Lee, K.H. Oh, T.W. Noh, R.A. De Souza, M. Martin, M. Kim, Unraveling the origin and mechanism of nanofilament formation in polycrystalline SrTiO₃ resistive switching memories, *Adv. Mater.* 31 (28) (2019) 1901322.
- [9] L.T. Kong, L.J. Lewis, Transition state theory of the preexponential factors for self-diffusion on Cu, Ag, and Ni surfaces, *Phys. Rev. B* 74 (7) (2006), 073412.
- [10] J. Koettgen, P.C. Schmidt, T. Bucko, M. Martin, Ab initio calculation of the migration free energy of oxygen diffusion in pure and samarium-doped ceria, *Phys. Rev. B* 97 (2) (2018), 024305.
- [11] M. Meyer, N. Nicoloso, MC-study of the anomalous conductivity of fluorite-type solid oxide solutions, *Ber. Bunsen Ges.* 101 (9) (1997) 1393–1398.
- [12] J.O. Nilsson, M. Leetmaa, O.Y. Vekilova, S.I. Simak, N.V. Skorodumova, Oxygen diffusion in ceria doped with rare-earth elements, *Phys. Chem. Chem. Phys.* 19 (21) (2017) 13723–13730.
- [13] A. Oaks, D. Yun, B. Ye, W.-Y. Chen, J.F. Stubbins, Kinetic Monte Carlo model of defect transport and irradiation effects in La-doped CeO₂, *J. Nucl. Mater.* 414 (2) (2011) 145–149.
- [14] S.B. Adler, J.W. Smith, J.A. Reimer, Dynamic monte-carlo simulation of spin-lattice relaxation of quadrupolar nuclei in solids - O-17 in yttria-doped ceria, *J. Chem. Phys.* 98 (9) (1993) 7613–7620.
- [15] P.P. Dholabhai, J.B. Adams, A blend of first-principles and kinetic lattice Monte Carlo computation to optimize samarium-doped ceria, *J. Mater. Sci.* 47 (21) (2012) 7530–7541.
- [16] P.P. Dholabhai, J.B. Adams, P.A. Crozier, R. Sharma, In search of enhanced electrolyte materials: a case study of doubly doped ceria, *J. Mater. Chem.* 21 (47) (2011) 18991–18997.
- [17] P.P. Dholabhai, S. Anwar, J.B. Adams, P. Crozier, R. Sharma, Kinetic lattice Monte Carlo model for oxygen vacancy diffusion in praseodymium doped ceria: applications to materials design, *J. Solid State Chem.* 184 (4) (2011) 811–817.
- [18] P.P. Dholabhai, S. Anwar, J.B. Adams, P.A. Crozier, R. Sharma, Predicting the optimal dopant concentration in gadolinium doped ceria: a kinetic lattice Monte Carlo approach, *Model. Simulat. Mater. Sci. Eng.* 20 (1) (2011), 015004.
- [19] R. Pornprasertsuk, J. Cheng, H. Huang, F.B. Prinz, Electrochemical impedance analysis of solid oxide fuel cell electrolyte using kinetic Monte Carlo technique, *Solid State Ionics* 178 (3–4) (2007) 195–205.
- [20] E. Lee, F.B. Prinz, W. Cai, Enhancing ionic conductivity of bulk single-crystal yttria-stabilized zirconia by tailoring dopant distribution, *Phys. Rev. B* 83 (5) (2011).
- [21] R. Krishnamurthy, Y.G. Yoon, D. Srolovitz, R. Car, Oxygen diffusion in yttria-stabilized zirconia: a new simulation model, *J. Am. Ceram. Soc.* 87 (10) (2004) 1821–1830.
- [22] G.E. Murch, Monte Carlo calculation as an aid in teaching solid-state diffusion, *Am. J. Phys.* 47 (1) (1979) 78.
- [23] A.F. Voter, Introduction to the kinetic Monte Carlo method, in: K.E. Sickafus, E. A. Kotomin, B.P. Uberuaga (Eds.), *Radiation Effects in Solids*, Springer Netherlands, Dordrecht, 2007, pp. 1–23.
- [24] S.A. Serebrinsky, Physical time scale in kinetic Monte Carlo simulations of continuous-time Markov chains, *Phys. Rev. E* 83 (3) (2011).
- [25] A. Chatterjee, D.G. Vlachos, An overview of spatial microscopic and accelerated kinetic Monte Carlo methods, *J. Comput. Aided Mater.* 14 (2) (2007) 253–308.

- [26] G. Murch, The haven ratio in fast ionic conductors, *Solid State Ionics* 7 (3) (1982) 177–198.
- [27] W.M. Visscher, Transport processes in solids and linear-response theory, *Phys. Rev. A* 10 (6) (1974) 2461–2472.
- [28] G.E. Murch, R.J. Thorn, Computer-simulation of ionic-conductivity - application to beta'-alumina, *Philos. Mag. A* 36 (3) (1977) 529–539.
- [29] B.O.H. Grope, T. Zacherle, M. Nakayama, M. Martin, Oxygen ion conductivity of doped ceria: a Kinetic Monte Carlo study, *Solid State Ionics* 225 (2012) 476–483.
- [30] S. Grieshammer, B.O.H. Grope, J. Koettgen, M. Martin, A combined DFT + U and Monte Carlo study on rare earth doped ceria, *Phys. Chem. Chem. Phys.* 16 (2014) 9974–9986.
- [31] J. Koettgen, T. Zacherle, S. Grieshammer, M. Martin, Ab initio calculation of the attempt frequency of oxygen diffusion in pure and samarium doped ceria, *Phys. Chem. Chem. Phys.* 19 (15) (2017) 9957–9973.
- [32] iCon: kinetic Monte Carlo. <http://icon.pc.rwth-aachen.de/>, 2020.
- [33] M. Matsumoto, T. Nishimura, Mersenne twister: a 623-dimensionally equidistributed uniform pseudo-random number generator, *ACM Trans. Model. Comput. Simulat.* 8 (1) (1998) 3–30.
- [34] R.A.Y. Fisher, Frank, *Statistical Tables for Biological, Agricultural and Medical Research*, Oliver and Boyd, London, 1948.
- [35] S. Grieshammer, S. Eisele, J. Koettgen, Modeling oxygen ion migration in the $\text{CeO}_2\text{-Y}_2\text{O}_3\text{-ZrO}_2$ solid solution, *J. Phys. Chem. C* 122 (33) (2018) 18809–18817.
- [36] R. Schmitt, J. Spring, R. Korobko, J.L.M. Rupp, Design of oxygen vacancy configuration for memristive systems, *ACS Nano* 11 (9) (2017) 8881–8891.
- [37] P.P. Dholabhai, J.B. Adams, A blend of first-principles and kinetic lattice Monte Carlo computation to optimize samarium-doped ceria, *J. Mater. Sci.* 47 (21) (2012) 7530–7541.
- [38] P.P. Dholabhai, J.B. Adams, P. Crozier, R. Sharma, Oxygen vacancy migration in ceria and Pr-doped ceria: a DFT+U study, *J. Chem. Phys.* 132 (9) (2010) 94104.
- [39] S. Grieshammer, S. Eisele, J. Koettgen, Modeling oxygen ion migration in the $\text{CeO}_2\text{-ZrO}_2\text{-Y}_2\text{O}_3$ solid solution, *J. Phys. Chem. C* 122 (33) (2018) 18809–18817.
- [40] A. Murray, G. Murch, C. Catlow, A new hybrid scheme of computer simulation based on Hades and Monte Carlo: application to ionic conductivity in Y_{3+} -doped CeO_2 , *Solid State Ionics* 18–19 (1986) 196–202.
- [41] M. Nakayama, M. Martin, First-principles study on defect chemistry and migration of oxide ions in ceria doped with rare-earth cations, *Phys. Chem. Chem. Phys.* 11 (17) (2009) 3241.
- [42] J. Koettgen, G. Dück, M. Martin, The oxygen ion conductivity of Lu doped ceria, *J. Phys. Condens. Matter* 32 (26) (2020) 265402.
- [43] J. Koettgen, M. Martin, The ionic conductivity of Sm-doped ceria, *J. Am. Ceram. Soc.* 103 (6) (2020) 3776–3787.
- [44] D. Krause, P. Thöring, JURECA: general-purpose supercomputer at Jülich supercomputing centre, *J. Large-Scale Res. Facil.* 2 (A62) (2016) A62.